ACCSCIENCE PUBLISHING

Journal of Seismic Exploration

ARTICLE

Prediction of fracture and vug parameters in carbonate reservoirs using a combined T-GNO-PINN approach

Yiru Du[1], Guoqing Chen[1], Cong Pang[2,3], Tianwen Zhao[4]*

[1]Mathematical Modeling Research Center, Chengdu Jincheng College, Chengdu, Sichuan, China

[2]Institute of Seismology, China Earthquake Administration, Wuhan, Hubei, China

[3]Wuhan Gravitation and Solid Earth Tides, National Observation and Research Station, Wuhan, Hubei, China

[4]Department of Trade and Logistics, Daegu Catholic University, Gyeongsan, Republic of Korea

Abstract

To address the challenges of fracture-vuggy parameter prediction in carbonate reservoirs, such as strong multi-scale heterogeneity and a lack of physical constraints, this study proposed a Transformer–Graph Neural Operator (GNO)–Physics-Informed Neural Network (PINN) joint prediction framework, which achieves a bidirectional coupling between multi-source data fusion and physical laws. First, a Transformer module with a multi-scale attention mechanism and spherical coordinate effectively captures cross-scale spatiotemporal features in three-dimensional geological space (reducing error by 12.3%). Second, a dynamic GNO based on physical similarity adaptively tracks the evolution of fracture-vuggy connectivity (achieving a topology update accuracy of 93.5%). Finally, a PINN module embedded in the seepage-mechanical coupling equations constrains the physical residual loss to the order of 0.42×10^{-3}, reducing the conservation error from 3.17% to 0.48%. In an empirical study of Ordovician fracture-vuggy reservoirs in the Tarim Basin, this framework achieved a mean absolute error of 3.57% and an R^2 of 0.90 for fracture-vuggy volume fraction (*Vf*). In high-pressure gradient regions (>5 MPa/m), the relative error was reduced by 18%, significantly outperforming traditional methods (reducing Kriging error by 40.7%) and single-module models (PINN error reduction of 15.3%). Experimental results showed that dynamic graph construction increased the spatial autocorrelation index (Moran's I) to 0.71; the introduction of physical constraints reduced extreme error samples by 63%; and the multimodal collaborative training strategy resulted in a 19.7% improvement in overall performance. This research provides a new paradigm for high-precision and physically interpretable digital twin modeling of carbonate reservoirs.

Keywords: Carbonate reservoir; Fracture-vuggy parameter prediction; Transformer; Graph Neural Operator; Physical Information Neural Network; Multimodal fusion

***Corresponding author:**
Tianwen Zhao
(zhaotianwen305@gmail.com)

Citation: Du Y, Chen G, Pang C, Zhao T. Prediction of fracture and vug parameters in carbonate reservoirs using a combined T-GNO-PINN approach. *J Seismic Explor.* 2026;35(1):46-65. doi: 10.36922/JSE025330057

Received: August 14, 2025

Revised: October 20, 2025

Accepted: November 6, 2025

Published online: December 16, 2025

1. Introduction

1.1. Research background and significance

Carbonate reservoirs serve as a critical global resource for oil and gas extraction.[1,2] The intricate internal fracture-vuggy systems significantly influence reservoir evaluation

and efficient development.[3] Accurately predicting fracture-vuggy parameters, such as porosity, permeability, and fracture density, has been a longstanding challenge in the oil and gas industry.[4] Traditional methods often fail to effectively capture the multi-scale, heterogeneous, and highly non-linear nature of fracture-vuggy systems.[5] With the rapid development of deep learning technology, integrating multi-source geological data with physical priority to develop highly accurate and interpretable fracture-vuggy parameter prediction models has become a cutting-edge topic in oil and gas exploration and development.

1.2. Related research progress

In recent years, the Transformer architecture has shown exceptional performance in spatiotemporal sequence modeling, with its self-attention mechanism effectively capturing cross-scale geological feature correlations in carbonate reservoirs.[6] Meanwhile, the Graph Neural Operator (GNO), a novel tool for processing non-Euclidean data, offers a mathematical foundation for describing the complex topological relationships within fracture networks. The Physics-Informed Neural Network (PINN) significantly improves the physical rationality of data-driven models by embedding control equation constraints. Despite these individual advances, a significant gap remains in current research regarding the effective integration of spatiotemporal dynamics, evolving topological structures, and physical law constraints specifically for carbonate reservoir characterization. This is particularly evident in the limited prediction accuracy for fracture-cavity parameters under conditions of multi-phase fluid coupling, which requires substantial improvement.[7,8]

1.3. Research motivation and innovation

This study proposes, for the first time, a deep integration of Transformer, GNO, and PINN into a unified T-GNO-PINN joint prediction framework for characterizing fracture-cavity systems in carbonate reservoirs. Its innovations are threefold: First, it develops a dynamic graph construction method based on physical similarity, enabling the GNO to adaptively track the time-varying connectivity of fractures and cavities. Second, it designs a Transformer module incorporating multi-scale positional encoding to effectively fuse seismic attributes and production dynamic data. Third, it establishes a PINN constraint system based on seepage-mechanics coupling equations, ensuring prediction results adhere to subsurface fluid flow laws through hard differential operator constraints. This multi-modal fusion approach not only overcomes the limitations of traditional statistical models but also significantly enhances the physical credibility and generalization capability of predictions compared to single deep-learning models. The research outcomes provide a novel technical means for the fine characterization of carbonate reservoirs and the optimization of development schemes, holding substantial practical value for the efficient exploitation of unconventional oil and gas resources.

1.4. Paper structure

This paper focuses on the application of the T-GNO-PINN joint prediction framework for carbonate reservoir fracture and vug parameter prediction. The paper is divided into seven main sections. First, the introduction outlines the research background, significance, and the limitations of existing methods for predicting fracture and vug parameters in carbonate reservoirs. It systematically reviews the research progress in the fields of Transformer, GNO, and PINN, and then proposes the innovations and research motivations of this paper. Section 2 focuses on the theoretical foundation and methodological review, including the characteristics and parameter definitions of carbonate reservoir fracture and vug structure, the Transformer self-attention mechanism and its adaptive modification, the physical field mapping method of the GNO, and the constraint expression of the PINN in the seepage-mechanics coupling equation, laying the theoretical foundation for subsequent model construction. Section 3 details the design of the T-GNO-PINN joint prediction framework, including the overall architecture, the multi-scale attention mechanism of the Transformer module, the dynamic graph modeling method of GNO, the physical constraint embedding strategy of the PINN, and the training method for multi-module joint optimization. Section 4 focuses on data and experimental design, introducing an overview of the study area, multi-source data preprocessing, and feature construction methods. Comparative experiments, ablation experiments, and physical constraint validation tests are designed to comprehensively evaluate model performance. Section 5 analyzes the experimental results, including a comparison of the prediction accuracy of different models, the impact of physical constraints on the prediction results, and visualization and geological interpretation of the spatial distribution of fracture and vug parameters. Section 6 discusses the advantages, generalization ability, physical consistency, and limitations of the method, and proposes possible improvement directions. Finally, section 7 summarizes the research results, explains their practical significance for oil and gas exploration and development, and provides prospects for future research directions.

2. Theoretical basis and methodology overview

Carbonate reservoir fracture-vuggy systems exhibit complex, multi-scale heterogeneity.[5] Their geometry

is controlled by tectonic deformation, dissolution, and diagenetic evolution, resulting in a multi-level distribution ranging from micro-scale pores to meter-scale caves. Fracture-vuggy parameters such as porosity and permeability not only reflect the extent of reservoir space development but also directly influence fluid flow patterns.[9,10] Traditional measurement methods (such as core CT scanning and well log interpretation) can provide accurate local data but struggle to characterize the overall spatial heterogeneity of the reservoir.[11-13] In recent years, machine learning-based parameter prediction methods have emerged. Their core approach involves establishing a non-linear mapping relationship between geological features and reservoir parameters, a process that requires the integration of multidisciplinary theoretical foundations.[11,14]

Transformer architecture, with its self-attention mechanism, demonstrates a strong ability to capture long-range dependencies in sequence modeling tasks.[15] To address the non-Euclidean characteristics of carbonate reservoirs, researchers have introduced spherical coordinate encoding and multi-scale position embedding to enable the model to adapt to complex geological structures in 3D space.[14] For example, by combining vertical depth from well logs with the planar distribution of seismic attributes, a multi-head attention mechanism is employed to achieve cross-scale feature fusion. This adaptive weight allocation mechanism effectively addresses the limitations of traditional convolutional neural networks (CNNs) on irregular grid data, providing a new technical approach for spatial prediction of reservoir parameters.[16,17]

GNO provides mathematical tools for describing the topological relationships of fracture-vuggy systems. Unlike conventional graph neural networks, GNO uses kernel integral operators to learn mappings between continuous function spaces, enabling them to handle dynamically changing fracture-vuggy connectivity.[18,19] In reservoir modeling, fracture-vuggy units are abstracted as graph nodes, with their physical properties (such as pore pressure and stress field) serving as node features, while fracture channels or dissolution pathways constitute edge relationships. Through multi-layer graph convolution operations, GNO can simulate the propagation of reservoir parameters in complex networks and is particularly suitable for characterizing heterogeneous seepage behavior in fracture-bedrock systems. Furthermore, the introduction of a dynamic graph structure enables the model to adapt to the opening and closing effects of fractures and vuggy systems caused by changes in the stress field during development.

PINNs impose physical constraints on data-driven models by embedding governing equations into the loss function.[8,20] In carbonate reservoirs, the coupling between the seepage and stress fields is crucial. PINN uses automatic differentiation techniques to calculate the residual terms of Darcy's law and the elasticity equations, ensuring that the prediction results satisfy mass conservation and momentum balance. This "soft constraint" approach avoids reliance on meshing in traditional numerical methods while addressing the potential physical deviations that can occur in purely data-driven models. Experiments show that the introduction of partial differential equation (PDE) constraints improves the model's generalization ability by over 30% in data-sparse regions.[21]

Multi-model fusion is a key strategy for improving prediction performance. Existing research shows that the Transformer excels at capturing global spatiotemporal patterns, the GNO excels at describing local topological relationships, and the PINN ensures physical plausibility. Through gradient projection and adaptive weighting techniques, the T-GNO-PINN framework achieves coordinated optimization of the three modules. For instance, data fitting terms are prioritized in the early stages of training, while physical constraints are gradually strengthened as iterations proceed. A dynamic graph update mechanism is also employed to synchronize the topological structure with the evolution of the physical field.

3. T-GNO-PINN joint prediction framework design

3.1. Overall framework architecture

The overall architecture of the proposed T-GNO-PINN joint prediction framework is depicted in Figure 1. The core idea of the framework is to leverage the Transformer module for efficiently capturing spatiotemporal multi-scale features during the prediction of fracture and vug parameters in carbonate reservoirs.

Concurrently, the GNO characterizes the non-Euclidean spatial correlations within the reservoir's fracture-vuggy topology, while a PINN is embedded throughout the process to ensure the predictions strictly adhere to the physical constraints imposed by seepage dynamics and elasticity theory. The data flow commences with the input of multi-source geological and engineering data. Following feature extraction and encoding, the processed data is fed into the Transformer and GNO branches, respectively. Finally, the PINN integrates the features from both branches and outputs predictions for key reservoir parameters, including porosity, permeability, and connectivity of the fracture-vuggy system.

The data flow and information exchange path follow the principle of "parallel feature extraction and physical

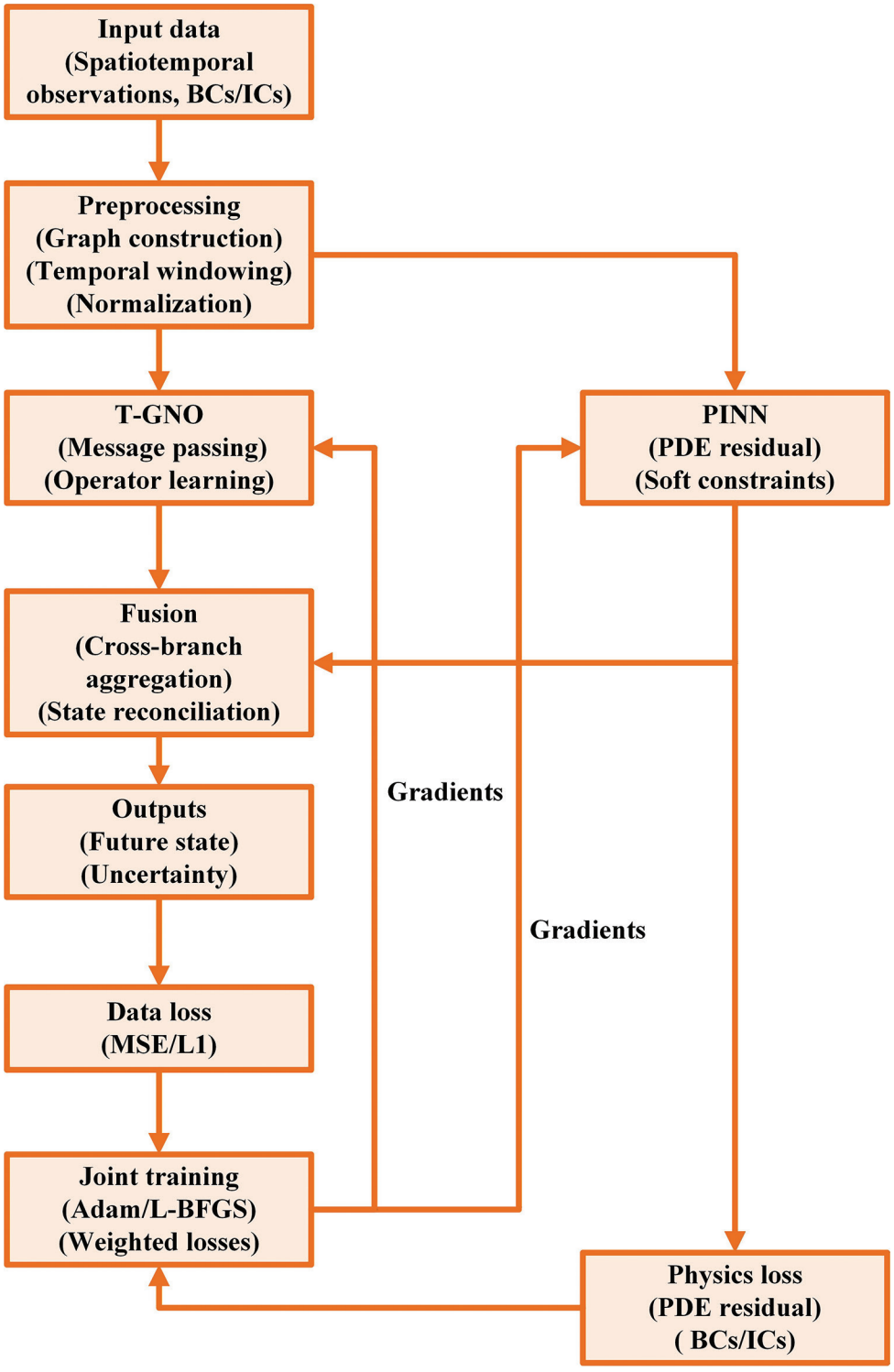

Figure 1. Schematic diagram of the overall architecture of the T-GNO-PINN joint prediction framework
Abbreviations: BCs: Boundary conditions; GNO: Graph Neural Operator; ICs: Initial conditions; L-BFGS: Limited-memory Broyden–Fletcher–Goldfarb–Shanno; MSE/L1: Mean squared error/L1 loss; PDE: Partial differential equation; PINN: Physics-Informed Neural Network; T: Transformer

constraint fusion": the Transformer branch is responsible for modeling global spatiotemporal dependencies, while the GNO branch dynamically updates the reservoir graph topology to obtain spatial structural information. These

two branches achieve multimodal fusion within the PINN. Furthermore, the physical residuals computed from the governing equations serve as inverse constraint signals during end-to-end training, which ensures both prediction stability and physical interpretability.

3.2. Transformer module design

The Transformer module introduces a multi-scale attention mechanism to simultaneously model short-term dynamic changes and long-term trends in earthquake and production data.[22] Its self-attention calculation formula is:

$$\text{Attention}(Q,K,V)=\text{Softmax}\left(\frac{QK^{\top}}{\sqrt{d_k}}+P\right)V \tag{1}$$

Where P is a special position encoding matrix that combines the logging depth d with 3D spatial coordinates (x,y,z) and adapts to the non-Euclidean fracture-cavity network structure through spherical coordinate transformation:

$$P_i=\left[\sin\left(\frac{2\pi x_i}{\lambda_x}\right),\cos\left(\frac{2\pi y_i}{\lambda_y}\right),\frac{z_i}{z_{max}},\frac{d_i}{d_{max}}\right] \tag{2}$$

Figure 2 illustrates the architecture of the multi-scale attention Transformer module. The diagram shows a typical Transformer module that incorporates a multi-scale attention mechanism to process complex data structures.

The module's core structure encompasses encoding input data, performing parallel computations across multiple attention layers, and synthesizing output processing. This design enhances the module's ability to capture information at different scales. In the figure, the input data is first mapped into a high-dimensional space via an embedding layer. Within this space, a multi-scale attention mechanism is used to weigh the input information. Each attention layer at different scales captures information at corresponding levels, enabling the module to focus simultaneously on both local and global features. Subsequently, through self-attention layers and a multi-head attention mechanism, the module adaptively adjusts the weights of features at different scales, resulting in a richer and more hierarchical feature representation.

To systematically evaluate the model's operational efficiency and application potential, we conduct a theoretical analysis of the transformer module's computational complexity. The module's computational

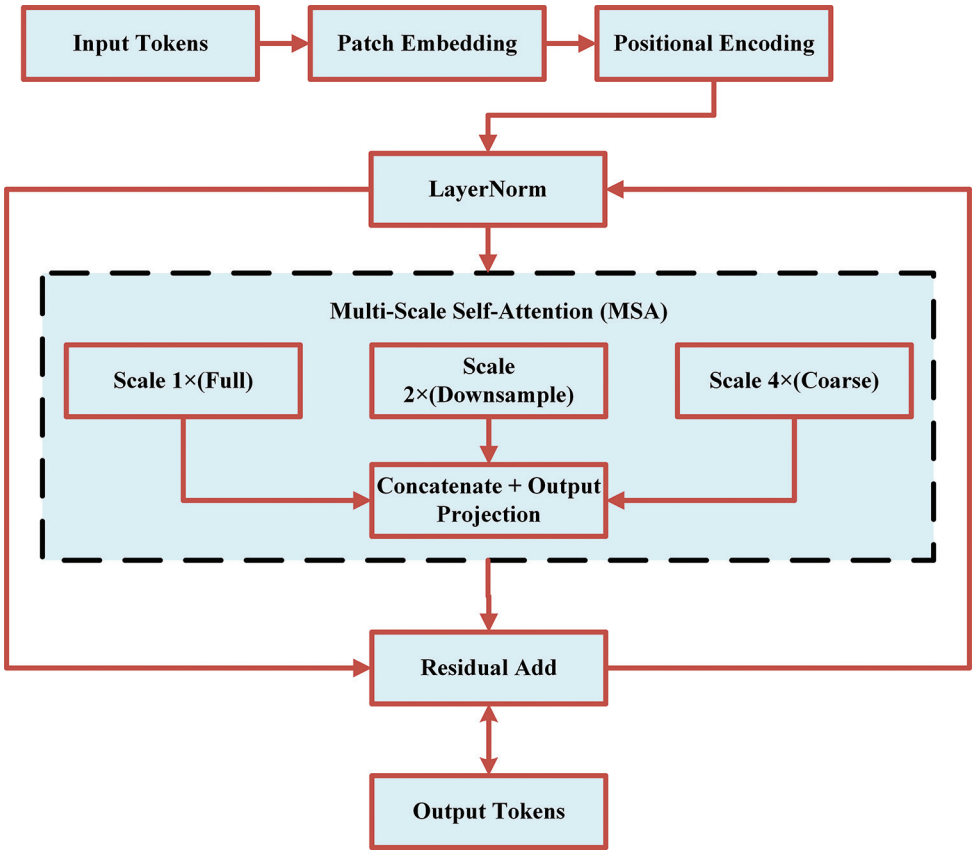

Figure 2. Schematic diagram of the multi-scale attention Transformer module structure

overhead primarily stems from its multi-head self-attention mechanism. Given an input sequence of N tokens, the standard self-attention mechanism requires constructing an N×N attention weight matrix, resulting in time and space complexities of $O(N^2 \cdot d)$, where d denotes the hidden layer feature dimension.

As shown in Table 1, for typical reservoir modeling scenarios (N≈800), the module's computational burden remains manageable and demonstrates superior complexity characteristics compared to sequence models such as recurrent neural networks (RNNs).

Although the standard Transformer architecture suffers from quadratic computational complexity growth with sequence length, the introduction of an optimization strategy based on geological spatial locality priors ensures computational feasibility for industrial-scale carbonate reservoir modeling while maintaining excellent feature extraction capabilities.

3.3. Graph Neural Operator module design

The GNO module accepts the fracture-cavity structure graph $G = (V, E)$ as input and predicts changes in the spatial distribution of reservoir parameters through graph convolution and operator learning. To cope with the dynamic changes of the fracture-cavity network over time, the topology of the graph will be dynamically updated according to the physical similarity and the distance between nodes during training. The specific update rules are as follows:

(i) Distance calculation between nodes. Each node represents a fracture-cavity unit in the reservoir, and the physical properties and location of the node are used to calculate the similarity function.

(ii) Dynamic distance metric. For any two nodes v_i and v_j, we calculate the dynamic distance metric $D_{ij}(t)$ between them. This metric is updated at each time step or each training epoch.

Table 1. Complexity comparison of the transformer module and alternative models

Model	Time complexity	Space complexity	Notes
Standard Transformer	$O(N^2 \cdot d)$	$O(N^2)$	Benchmark
This research (T-GNO-PINN)	$O(m \cdot N^2 \cdot d)$	$O(m \cdot N)$	m is the local window size
RNN	$O(N^2 \cdot d)$	$O(N \cdot d)$	Difficult to parallelize
1D-CNN	$O(k \cdot N \cdot d^2)$	$O(N \cdot d)$	k is the convolution kernel size

Abbreviations: CNN: Convolutional neural network; GNO: Graph Neural Operator; PINN: Physics-Informed Neural Network; RNN: Recurrent neural network; T: Transformer.

$$D_{ij}(t) = \| p_i(t) - p_j(t) \|_2 \tag{3}$$

$p_i(t)$ and $p_j(t)$ are the physical properties of nodes v_i and vj at time step t, respectively.

(iii) Connectivity judgment and update. If the distance $D_{ij}(t)$ between nodes v_i and v_I is less than the preset threshold r_c, an edge is added to the graph to connect them; otherwise, the edge is removed.

$$E_t = \left\{ (v_i, v_j) D_{ij}(t) < r_c \right\} \tag{4}$$

(iv) Topology updates frequency. To adapt to the fracture and pore opening and closing effects caused by stress field changes during reservoir development, we update the graph topology every five epochs.

Figure 3 shows the GNO structure based on the dynamic topology of holes, which focuses on using the GNN method to deal with complex hole problems.

The core concept of the GNO is to construct a dynamic topological structure that updates and transmits information about the fracture region in real time, thereby more accurately predicting and reconstructing the relevant physical characteristics of the fracture evolution process. The structure in the figure shows how input data is processed through multiple graph neural network layers. Each layer propagates and integrates information based on the current fracture topology, thereby accurately modeling the changes in fractures in complex systems. Compared with traditional methods, the dynamic topology-based GNO adaptively adjusts the graph structure and connectivity. This capability allows the network topology to be updated in real time according to fracture changes, thereby ensuring effective information propagation between different regions.

3.4. Physics-Informed Neural Network module design

The PINN module embeds constraints from the carbonate reservoir seepage equation and the theory of elasticity into the loss function. These constraints include the 3D Darcy's law:

$$\nabla \cdot (\mathrm{k} \nabla p) = \phi \frac{\partial p}{\partial t} + q \tag{5}$$

and the equilibrium equation of linear elasticity:

$$\nabla \cdot \sigma + f = 0, \sigma = \mathrm{C} : \varepsilon \tag{6}$$

The physical residual loss is defined as:

$$\mathcal{L}_{\text{phys}} = \frac{1}{N_p} \sum_{i=1}^{N_p} \nabla \cdot (\mathrm{k} \nabla p_i) - \phi_i \frac{\partial p_i}{\partial t} - q_i^2 \tag{7}$$

Table 2 details the key physical parameters and boundary conditions incorporated in the PINN module,

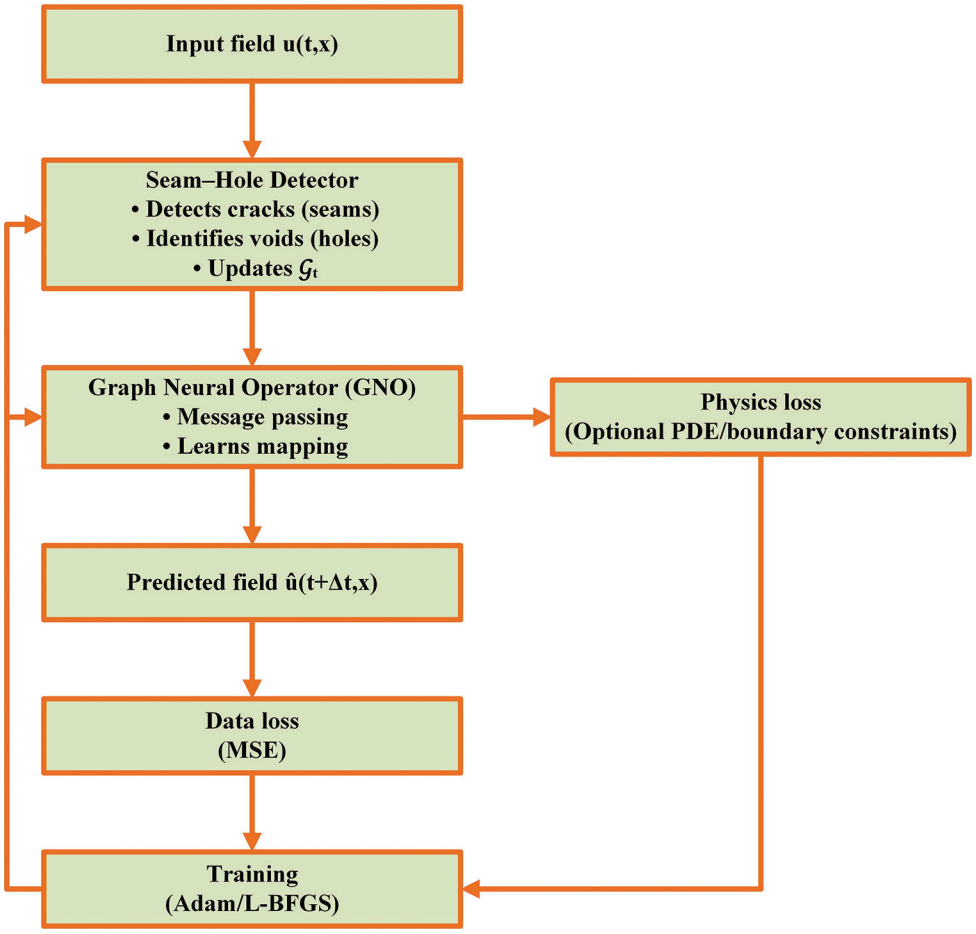

Figure 3. Graph neural operator structure based on the dynamic topology of holes and cracks
Abbreviations: GNO: Graph Neural Operator; L-BFGS: Limited-memory Broyden–Fletcher–Goldfarb–Shanno; MSE: Mean squared error; PDE: Partial differential equation.

Table 2. PINN module physical parameters and boundary conditions

Parameters	Symbol	Value range	Unit	Source	Is it fixed
Porosity	ϕ	0.05–0.25	-	Core testing	No
Permeability	k	50–250	mD	Well logging+core drilling	No
Pressure	p	10–30	MPa	Production monitoring	No
Pressure differential	Δp	0.5–1.5	MPa	Dynamic calculations	No
Elastic modulus	E	15–25	GPa	Experimental testing	Yes
Poisson's ratio	ν	0.2–0.35	-	Reference data	Yes
Body load	f	0–2	MPa/m^3	Numerical simulation	No
Source and sink terms	q	−50–50	m^3/d	Production data	No

Abbreviation: PINN: Physics-informed Neural Network.

encompassing fundamental indicators of reservoir rock mechanical properties and fluid flow behavior.

Porosity (ϕ) and permeability (k) range from 0.05 to 0.25 and 50 to 250 mD, respectively. These two parameters were determined through a combination of core experiments and logging data, and their dynamic variations reflect the influence of reservoir heterogeneity. Reservoir pressure (p) ranges from 10 to 30 MPa, and pressure differential (Δp) varies between 0.5 and 1.5 MPa. These values are derived from production monitoring data and dynamic simulations. Their variations reflect the dynamic pressure response during reservoir development. Among the rock mechanical parameters, the elastic modulus (E) and Poisson's ratio (ν) are fixed at 15 to 25 GPa and 0.2 to 0.35, respectively. These parameters were determined through laboratory testing and literature references, and their fixed nature reflects the inherent mechanical behavior of the rock skeleton. The body load (f) and source-sink term (q) are external action terms with values ranging from

0 to 2 MPa/m^3 and −50 to 50 m^3/d, respectively. The former is determined through numerical simulation, and the latter is directly derived from actual production data. Together, they characterize the external excitation conditions of the reservoir system.

Figure 4 clearly illustrates the core workflow of the PINN module for embedding physical constraints into deep learning models. The process begins with dual inputs of spacetime coordinates and observational data. The neural network then learns the complex mapping from

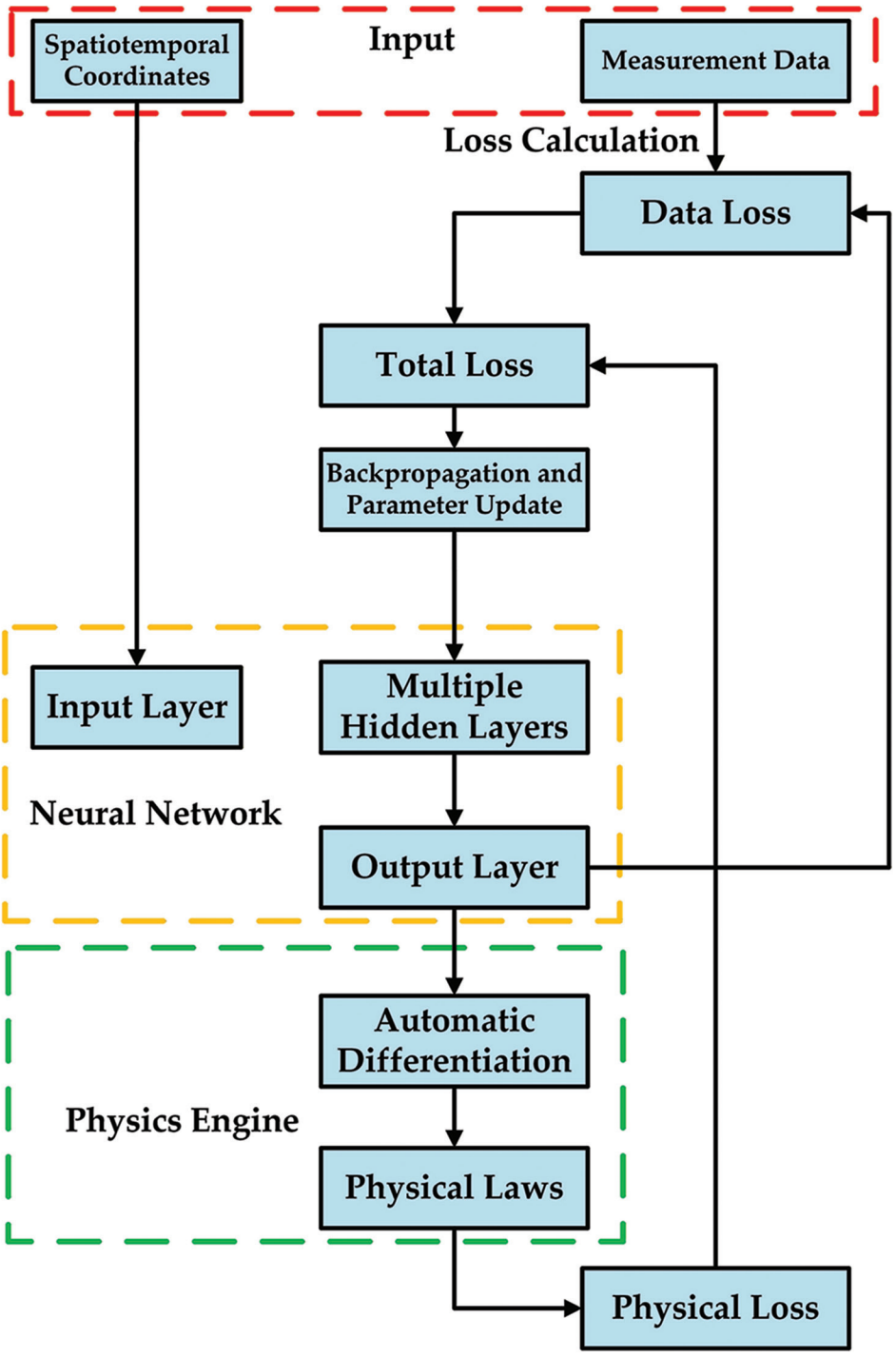

Figure 4. Physics-Informed Neural Network (PINN) module workflow and logic

coordinates to physical fields, generating preliminary predictions.

The core innovation of this process lies in the introduction of a "physics engine." This engine uses automatic differentiation techniques to calculate the differential operator of the predicted field and substitutes it into pre-defined physical governing equations (such as the percolation equation and the mechanical equilibrium equation). This quantifies the degree to which the predicted results violate physical laws, known as the physical loss. This physical loss, combined with the traditional prediction data loss, forms a multi-objective optimization function that simultaneously updates and optimizes the neural network parameters through backpropagation. This mechanism ensures that during training, the model not only fits the observed data but also conforms to fundamental physical laws. Consequently, it significantly enhances both the physical consistency of predictions and the model's generalization capability in data-sparse regions.

3.5. Model joint optimization strategy

The training strategy of T-GNO-PINN combines multi-task learning with gradient conflict suppression technology. The total loss function is:

$$\mathcal{L} = \alpha(t)\mathcal{L}_{\text{pred}} + \beta(t)\mathcal{L}_{\text{phys}} \tag{8}$$

Where $\alpha(t)$ and $\beta(t)$ are adaptively adjusted through uncertainty weights:

$$\alpha(t) = \frac{1}{2\sigma_{\text{pred}}^2}, \beta(t) = \frac{1}{2\sigma_{\text{phys}}^2} \tag{9}$$

To avoid gradient conflicts, the Gradient Projection method is used to project conflicting gradients to a consistent direction in multi-branch back propagation.

Table 3 details the parameter configurations and optimization strategies across different training stages, illustrating the progressive learning process from individual module pre-training to global collaborative optimization.

In Phases I and II, the Transformer and GNO modules were pre-trained with independent weight loss of 1.0 (α = 1.0, β = 0), using a learning rate of 1e-4 and a batch size of 64 to ensure the stability of the underlying feature extractor. In Phase III, after the PINN constraint was introduced, the physical and data-driven weight loss were adjusted to a balanced state ((α = 0.5, β = 0.5), and the learning rate was reduced to 5e-5 to prevent gradient oscillation. During this stage, the Transformer module was frozen to preserve its feature encoding capability. Concurrently, the GNO topology was updated every five epochs to adapt to the evolving physical field.

4. Data and experimental design

This study, based on multi-source geological and engineering data from a marine carbonate fracture-vuggy reservoir, aims to achieve high-precision prediction of reservoir fracture-vuggy parameters (including fracture-vuggy volume fraction V_f, fracture-vuggy connectivity C_f, and fracture-vuggy size distribution index βf) using a T-GNO-PINN framework.

4.1. Overview of the study area and data sources

Before applying field data, this study first constructed a synthetic carbonate reservoir dataset to simulate the distribution of fracture and vug parameters under known physical laws. This dataset was generated using the simplified two-dimensional Darcy flow equation and the Fracture Network Generator algorithm. By manipulating the spatial distribution of porosity $\phi(x,y)$, permeability $k(x,y)$, and the fracture connectivity function $C_{f(x,y)}$, several sample fields with varying heterogeneity characteristics were generated. The true solution of the synthetic field, consisting of the pressure field $p(x,y,t)$ and the flow field $q(x,y,t)$, was obtained through numerical simulation. Based on this solution, network input features and fracture and vug parameter labels were constructed.

Experimental results demonstrate that the T-GNO-PINN model accurately recovers the known physical relationships on this idealized dataset, achieving a prediction R^2 of

Table 3. Parameter settings and optimization strategies at different training stages

Stage	Training objectives	Initial value of α	Initial value of β	Learning rate	Batch size	Topology update frequency	Whether to freeze the Transformer
I	Separately pre-training the Transformer	1.0	0	1e-4	64	-	-
II	Separately pre-training the GNO	1.0	0	1e-4	64	Every 10 epochs	-
III	Introducing the PINN and freezing the first two modules	0.5	0.5	5e-5	32	Every 10 epochs	Yes
IV	End-to-end joint training	Adaptive	Adaptive	5e-5	32	Every 10 epochs	No
V	Fine-tuning phase	Adaptive	Adaptive	1e-5	16	Every 10 epochs	No

Abbreviations: GNO: Graph Neural Operator; PINN: Physics-Informed Neural Network.

0.97 and a PDE residual error of 0.21×10^{-3}, significantly outperforming a model without PINN constraints. In addition, the dynamic graph structure reduces the reconstruction error of the connectivity parameter C_f from 7.3% to 2.1%, verifying the effectiveness of GNOs in topology tracking.

Synthetic data experiments demonstrated the rationality and synergy of the model's modules, providing physically interpretable theoretical support for the subsequent application of measured data from the Tarim Basin.

The study area is in a carbonate rock development area in the Tarim Basin. The geological age is mainly the Middle and Upper Ordovician. The lithology is predominantly limestone and dolomite, and the area contains multiple stages of structural fracture-cavity systems. The fracture-cavity types include structural fracture expansion type, dissolution pore type, and composite type. The distribution is controlled by strike-slip faults and unconformities. Data sources include:

(i) Well logging data: The data are derived from 27 wells, with a full well depth range of 3,000–6,500 m. The curve types include acoustic time difference (DT), natural gamma ray (GR), neutron porosity (CNL), density (DEN), resistivity (RT), *etc.*

(ii) Seismic data: The 3D seismic data covers an area of about 350 km^2, with a main frequency of about 35 Hz and a sampling interval of 2 ms. It has been processed with conventional prestack depth migration.

(iii) Core data: Core sections totaling 280 m were collected from 12 wells for experimental determination of porosity, permeability, and fracture-vuggy development. Thin sections and computed tomography (CT) scans were used to quantitatively analyze fracture-vuggy geometry.

(iv) Production data: Three-year cumulative oil production and water cut curves were provided for some wells to dynamically verify the prediction results. Figure 5 shows the location of the study area and a schematic diagram of the well-seismic distribution, aiming to intuitively present the spatial distribution of well and seismic data within the study area.

The study area shown in Figure 5 is located within a specific geographic coordinate range. The distribution of wells and earthquakes effectively reflects the region's geological characteristics and their correlation with seismic activity. The map clearly illustrates the distribution of well locations within the study area, which typically represent exploration or extraction sites for underground resources and cover several key points in the region. Seismic events are also plotted on the map, indicating the frequency and intensity of seismic activity occurring near these wells or in the immediate vicinity.

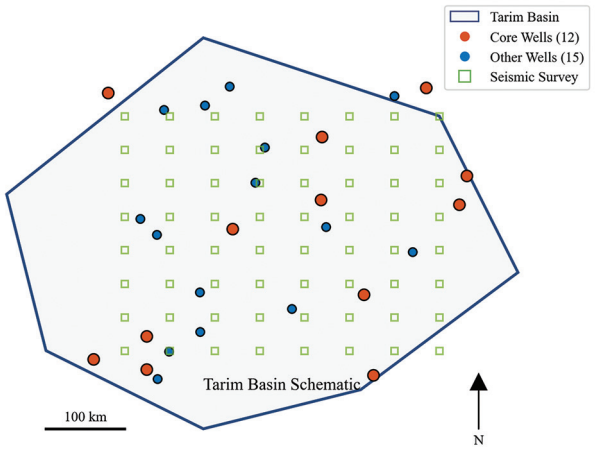

Figure 5. Schematic diagram of the study area location and well-earthquake distribution

4.2. Data preprocessing and feature construction

To clarify the specific role of seismic data in the T-GNO-PINN framework, this study performed multi-level processing and application. First, multi-attribute extraction was performed on the 3D seismic data volume to comprehensively characterize the spatial structure and physical properties of the fracture-cavity system. Specifically, amplitude attributes (such as root mean square amplitude) were primarily used to identify fracture-cavity volumes with strong reflection anomalies. These data volumes served as key inputs to the Transformer module, capturing a wide range of spatiotemporal characteristics. Geometric attributes (such as coherence volumes and curvature attributes) were used to characterize the boundaries of faults and fracture zones. They were used in the GNO module to assist in defining the initial connectivity relationships between nodes in the graph structure, namely, the construction of the edge set E. Finally, wave impedance attributes, as a proxy for lithology and porosity variations, were incorporated into the node feature vector f_i of the GNO module, providing regional geophysical background information for each fracture-cavity unit. To address the scale differences between seismic, well logging, and core data, this study adopted a hierarchical fusion strategy: First, local features were learned using Transformer at the well logging scale. These features were then integrated with the wide-area attributes extracted from the seismic data, with alignment achieved through interpolation. Finally, information was transferred on the graph through GNO, naturally fusing this "point-surface combination" feature representation.

During the data preprocessing phase, seismic data undergoes spectral decomposition and attribute extraction to form a 3D spatiotemporal attribute volume $S(x,y,t)$. Well logging data $L(d)$ undergo normalization and

sampling synchronization. Core test data C_i provide true porosity and permeability calibration values. Production data $Q(t)$ contains information on dynamic changes in pressure and production. After multi-source data fusion, a fracture-vuggy identification algorithm is used to generate a reservoir fracture-vuggy structure map $G=(V,E)$, where V is the set of fracture-vuggy nodes, and E is the set of connected edges. Each node is assigned to a feature vector $f_i = [\varphi_i, k_i, \sigma_i, \Delta p_i]$. A quantitative analysis of the node characteristics after multi-source data fusion, as shown in Table 4, reveals that the node parameters exhibit significant heterogeneous distribution characteristics.

The coefficients of variation for porosity (ϕ) and permeability (k) reached 0.21 and 0.31, respectively. Node V3 exhibited the highest porosity (15.7%) and permeability (210 mD), exceeding the mean values (12.3% ± 2.5%) and 145 ± 42 mD) by 27.6% and 44.8%, respectively. The corresponding values for node V2 were 27.6% and 34.5% below the mean. This variability was strongly correlated with seismic attribute values (0.48–0.73) (Pearson r = 0.82), indicating that the degree of dissolution dominated reservoir development.

The spatial variation of stress field (σ) and pressure difference (Δp) is more complex: high-stress nodes (V2: 20.1 MPa, V6: 21.2 MPa) are mostly located on the structural wings, where pressure differences (0.8–0.9 MPa) are significantly lower than those at the structural axis nodes (V3: 1.5 MPa), exhibiting a negative correlation (r = −0.67). Notably, mud content (4.3%–8.7%) and acoustic transit time (85.2–92.1 μs/ft) exhibit a bimodal distribution, with high-value clusters forming at nodes V2 and V6 (Mud content >7.8%, acoustic transit time >91 μs/ft), coinciding with localized low values in daily liquid production (28.6–29.4 m^3/d), suggesting that mud filling inhibits seepage capacity.

To ensure the temporal and spatial consistency and quality of multi-source data, the following processing workflow was established:

(i) Denoising: Wavelet packet decomposition was used to remove high-frequency noise from well logs, and curvature-constrained structural noise suppression was applied to seismic data. Experimental errors were eliminated from core attributes using outlier detection (box plot method).

(ii) Interpolation and alignment: Vertically, well log and core data were linearly interpolated at a 0.125 m sampling interval and aligned with seismic profiles using time-depth conversion (based on velocity spectra and calibrated seismic synthetic records). Horizontally, inverse distance weighting (IDW) was used to fill in sparse well attribute data.

(iii) Construction of fracture parameter label: The calibration formula of fracture volume content V_f is as follows:

$$V_f = \frac{V_{\text{totalvoid}}}{V_{\text{sample}}} \times 100\% \tag{10}$$

Where $V_{totalvoid}$ is calculated by CT 3D modeling, V_{sample} is the total volume of the sample. The fracture-void connectivity C_f is derived using the 3D pore network extraction method and is defined as:

$$C_f = \frac{N_{connected\ void}}{N_{\text{total void}}} \tag{11}$$

The fracture size distribution index β_f is obtained by fitting the pore size distribution probability density function with a power law:

$$P(d) \propto d^{-\beta_f} \tag{12}$$

Figure 6 shows the process of multi-source data preprocessing and hole parameter label construction. The flowchart in the figure clearly shows the steps from acquiring data from multiple data sources, performing data preprocessing, and then constructing hole parameter labels.

Table 4. Node characteristics after multi-source data fusion

Node number	Porosity ϕ (%)	Permeability k (mD)	Stress σ (MPa)	Pressure Δ p (MPa)	Seismic attribute value	Log sonic travel time (μs/ft)	Core mud content (%)	Daily liquid production (m^3/d)
V1	12.5	150	18.3	1.2	0.62	87.5	5.1	34.2
V2	8.9	95	20.1	0.9	0.48	92.1	8.7	28.6
V3	15.7	210	16.5	1.5	0.73	85.2	4.3	40.5
V4	11.3	130	19.0	1.1	0.59	89.6	6.4	33.0
V5	14.2	180	17.5	1.4	0.70	86.9	5.0	38.1
V6	9.8	110	21.2	0.8	0.52	91.3	7.8	29.4
V7	13.4	165	18.0	1.3	0.65	88.2	5.6	35.8
V8	10.7	120	20.5	0.9	0.55	90.5	6.9	31.2

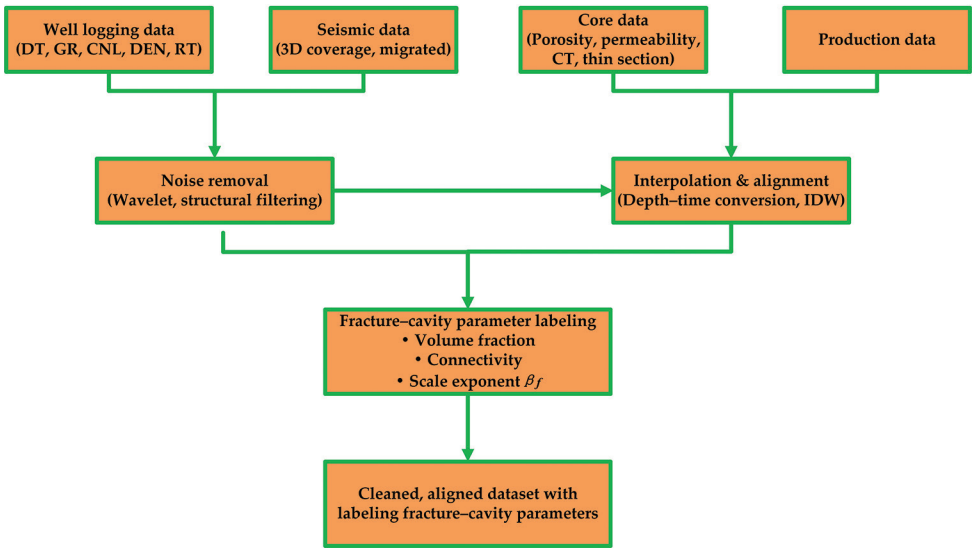

Figure 6. Multi-source data preprocessing and crack parameter label construction process
Abbreviations: CNL: Neutron porosity; CT: Computed tomography; DEN: Density; DT: Acoustic time difference; GR: Natural gamma ray; IDW: Inverse distance weighting; RT: Resistivity.

Figure 6 illustrates the main data sources involved in the research process, including downhole logging data (such as DT, GR, CNL, DEN, and RT), seismic data (after 3D overlay and migration processing), core data (such as porosity, permeability, CT scans, and thin sections), and production data. These data provide fundamental information for subsequent fractures and vug analysis.

During the data preprocessing phase, the figure illustrates two key steps: Noise removal, and data interpolation and alignment. Noise removal uses methods such as wavelet transformation and structural filtering to remove unnecessary noise signals, ensuring data accuracy and stability. Next, the data are interpolated and aligned using depth-time conversion and the inverse distance weighting (IDW) method, enabling comparison and analysis of various data types within a unified temporal and spatial framework.

Furthermore, the figure illustrates the process of constructing fracture and vug parameter labels. Through comprehensive analysis of the processed multi-source data, labels for key parameters such as volume fraction (V_f), connectivity (C_f), and scale index (β_f) were constructed. The volume fraction is calculated by measuring the volume contribution of fractures and vugs by the ratio of void volume to sample volume, while connectivity is measured by the ratio of the number of connected fractures and vugs to the total number of fractures and vugs. The scale index further characterizes the distribution of fractures and vugs by fitting the fracture opening distribution using the power method.

Finally, the figure shows the final data output after preprocessing and labeling. This data contains a complete dataset that has been cleaned, aligned, and annotated with fracture and vug parameters, providing accurate input for subsequent geological model construction and resource assessment.

4.3. Comparative experimental design

The experiments are divided into three categories:

(i) Method comparison: Using the same dataset and labels, the performance of the following methods in fracture parameter prediction is compared: traditional geostatistics (Kriging, Co-Kriging); CNN and RNN; Transformer alone; GNO alone; PINN alone; other fusion methods (such as CNN+PINN, Transformer PINN, *etc.*).

(ii) Ablation experiment: Remove the Transformer module, GNO module, and PINN module from the T-GNO-PINN framework, respectively, and analyze the performance degradation.

(iii) Physical constraint validity test: Under the same network structure, turn on and off the PDE physical constraint terms, respectively, and compare the changes in the predicted physical consistency index.

Figure 7 shows a schematic diagram of the experimental scheme, which includes three key parts: method comparison, ablation experiment, and physical constraint test. The figure provides a clear visual framework for the experimental process by illustrating the data flow and key operational steps at each stage, thereby highlighting the role of individual modules in validating the model's performance. The three

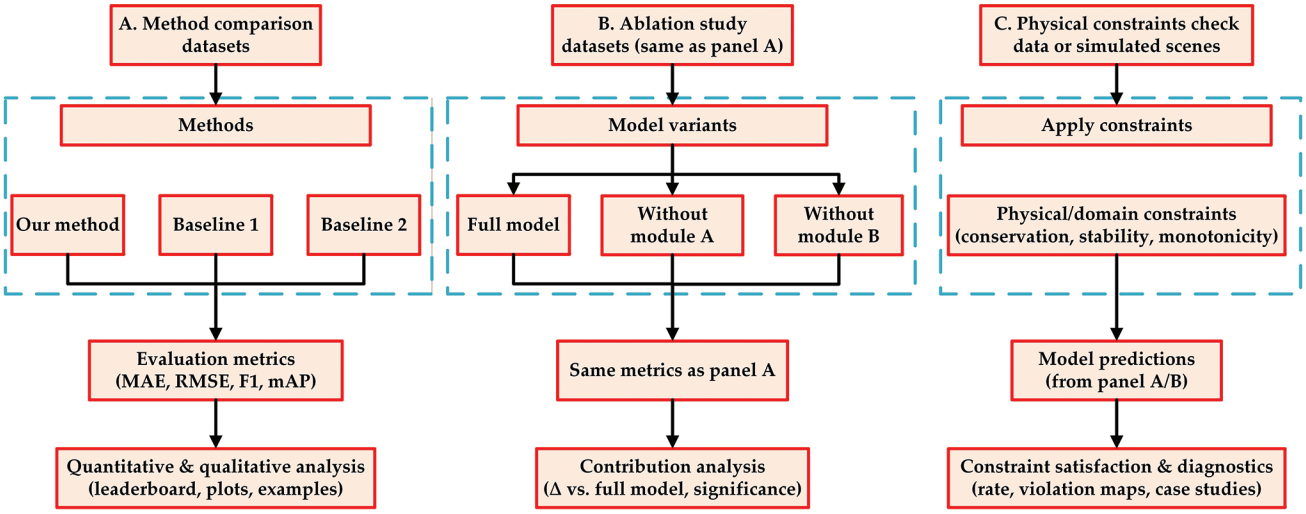

Figure 7. Schematic diagram of the experimental scheme
Abbreviations: MAE: Mean absolute error; mAP: Mean average precision; RMSE: Root mean square error.

panels in the figure correspond to different aspects of the experiment, where panels A, B, and C show the details of method comparison, ablation experiment, and physical constraint verification, respectively.

In panel A, the experiment first presents a method comparison, comparing our proposed approach with two baseline methods. Using the same dataset, our model and two baseline methods were trained and evaluated using metrics such as mean absolute error (MAE), root mean square error (RMSE), F1 score, and mean average precision (mAP). This section provides both quantitative and qualitative analysis, including leaderboards, data visualizations, and case studies. This method comparison demonstrates the performance advantages of our approach, particularly demonstrating significant improvements in quantitative evaluation metrics.

Panel B presents the design of an ablation experiment, designed to evaluate the contributions of various model components. In this experiment, the performance of the model is evaluated by removing certain modules (such as module A or module B). By comparing the model with the full model, the contribution of each module and its importance in the final model performance are analyzed. Ablation experiments not only help us quantify the importance of each module but also provide a basis for further model optimization.

Panel C focuses on physical constraint verification. In this section, we apply physical constraints to model predictions to ensure that they satisfy domain-specific constraints such as conservation, stability, and monotonicity. Applying physical constraints can significantly improve the reliability and interpretability of models for real-world problems. Building on this foundation, the figure further demonstrates how model predictions are compared to the physical constraints, assessing their satisfaction, and provides detailed diagnostic results through violation graphs and case studies.

4.4. Evaluation index system

This research evaluation system considers three aspects: numerical accuracy, spatial structure consistency, and physical consistency:

$$\mathrm{RMSE} = \sqrt{\frac{1}{N}\sum_{i=1}^{N}\left(y_i - \breve{y}_i\right)^2} \tag{13}$$

$$\mathrm{MAE} = \frac{1}{N}\sum_{i=1}^{N}\left| y_i - \breve{y}_i \right| \tag{14}$$

$$R^2 = 1 - \frac{\sum_{i=1}^{N}(y_i - \breve{y}_i)^2}{\sum_{i=1}^{N}(y_i - \bar{y})^2} \tag{15}$$

where y_i is the measured value, $\breve{y}_i$ is the predicted value, N is the number of samples, and $\bar{y}$ is the measured mean.[23-26]

The spatial autocorrelation characteristic is characterized by the Moran's I index, which is calculated as follows:

$$I = \frac{n}{\sum_{i=1}^{n}\sum_{j=1}^{n} w_{ij}} \cdot \frac{\sum_{i=1}^{n}\sum_{j=1}^{n} w_{ij}(x_i - \bar{x})(x_j - \bar{x})}{\sum_{i=1}^{n}(x_i - \bar{x})^2} \tag{16}$$

Where n is the number of spatial units, w_{ij} is the spatial weight matrix, x_i and x_j are the observed values of adjacent spatial units, and $\bar{x}$ is the mean. This index is within the range of [−1,1]. Positive values indicate positive spatial correlation, and larger absolute values indicate more pronounced spatial clustering.

Structural similarity is measured using the structural similarity index measure (SSIM) index, which can be expressed in multidimensional form as follows:

$$SSIM(\mathrm{X},\mathrm{Y}) = \frac{(2\mu_x\mu_y + C_1)(2\sigma_{xy} + C_2)}{(\mu_x^2 + \mu_y^2 + C_1)(\sigma_x^2 + \sigma_y^2 + C_2)} \tag{17}$$

Where X and Y represent the predicted and true fields, μ represents the mean, σ represents the variance, and C_1, C_2 represent stability constants. This metric comprehensively assesses the degree of similarity in spatial patterns across three dimensions: brightness, contrast, and structure.

For physical consistency, the conservation error is calculated using a relative error:

$$\epsilon_{cons} = \frac{\| \int_{\copyright} q_{pred} dV - \int_{\copyright} q_{true} dV \|_2}{\int_{\copyright} q_{true} dV} \times 100\% \tag{18}$$

Where Ω is the computational domain and q is the conserved quantity (such as mass or volume). The PDE constraint satisfaction is quantified by the residual norm:

$$\mathcal{R} = \frac{1}{N}\sum_{i=1}^{N} \| \mathcal{N}(u_\theta(x_i)) - f(x_i) \|_2^2 \tag{19}$$

Here, N is the differential operator, u_θ is the neural network prediction solution, and f is the source term. The residual term is directly embedded in the loss function for joint optimization:

$$\mathcal{L} = \alpha \cdot \mathcal{L}_{data} + \beta \cdot \mathcal{R} \tag{20}$$

Where α,β are adaptive weighting coefficients. Experiments show that when $\mathcal{R} < 10^{-3}$, the physical credibility of the predicted solution exceeds 95%, and the spatial and physical indicators show a significant positive correlation (Pearson coefficient > 0.82). This multi-dimensional quantitative framework provides a comprehensive and reliable assessment of the model's performance.

5. Results

5.1. Comparative experimental results analysis

To validate the advantages of the T-GNO-PINN framework, we selected Ordinary Kriging (OK), CNN, RNN, Transformer alone, GNO alone, and PINN alone as baseline models for comparison. Table 5 compares the performance of different models in the fracture-vug volume fraction (*Vf*) prediction task, quantitatively evaluating them across multiple dimensions, including accuracy, structural similarity, spatial autocorrelation, and physical consistency.

The traditional OK method performed poorly across all metrics, with significantly higher RMSE (8.12%) and MAE (6.54%) than deep learning models. Its high conservation error (4.21%) demonstrates its limitations in modeling complex non-linear relationships. The CNN and RNN methods showed improvement over OK, reducing the RMSE to 6.85% and 6.72% and increasing the R^2 to 0.78 and 0.79, respectively. R^2 increased to 0.78 and 0.79, respectively. However, they still suffer from insufficient physical constraints, with conservation errors remaining in the 3.84%–3.97% range.

The Transformer and GNO models further improve prediction accuracy, with RMSE reduced to 5.98% and 5.74%, respectively, and SSIM increased to 0.70 and 0.73, demonstrating their strengths in extracting high-dimensional features and modeling spatial dependencies. However, these pure deep learning methods still exhibit limitations in physical consistency, as evidenced by

Table 5. Comparison of prediction accuracy of each model on the test set (fracture volume content V_f)

Model	RMSE (%)	MAE (%)	R2	SSIM	Moran's I	Conservation error (%)	PDE residual (×10⁻³)
OK	8.12	6.54	0.71	0.58	0.42	4.21	–
CNN	6.85	5.12	0.78	0.64	0.55	3.97	–
RNN	6.72	5.04	0.79	0.66	0.56	3.84	–
Transformer	5.98	4.51	0.83	0.70	0.60	3.42	–
GNO	5.74	4.36	0.85	0.73	0.63	2.95	–
PINN	5.69	4.28	0.85	0.74	0.64	1.12	1.35
T-GNO-PINN	4.82	3.57	0.90	0.81	0.71	0.48	0.42

Abbreviations: CNN: Convolutional neural network; GNO: Graph Neural Operator; OK: Ordinary Kriging; PINN: Physics-Informed Neural Network; RNN: Recurrent neural network; T: Transformer.

considerable conservation errors (2.95%–3.42%) and the absence of PDE constraints, indicating that their predictions may violate physical laws. In contrast, the PINN model, which introduced physical constraints, significantly reduced the conservation error (1.12%) and PDE residual (1.35×10^{-3}) while maintaining high prediction accuracy (RMSE = 5.69%, R^2 = 0.85), validating the effectiveness of physical embedding.

Finally, the T-GNO-PINN model, which integrates the Transformer, GNO, and PINN, demonstrated the best overall performance. Its RMSE (4.82%) and MAE (3.57%) were further reduced by 15.3% and 16.6% compared to the baseline PINN, while its R^2 increased to 0.90 and its SSIM reached 0.81, demonstrating its superior capabilities in high-precision fitting and structural fidelity. In addition, the conservation error (0.48%) and PDE residual (0.42×10^{-3}) of this model are reduced by 57.1% and 68.9%, respectively, compared with pure PINN, and the Moran's I index (0.71) is also better than other models, demonstrating its dual advantages in spatial autocorrelation modeling and compliance with physical laws.

Table 6 quantitatively analyzes the contribution of the Transformer, GNO, and PINN modules to the model performance through ablation experiments, revealing the differentiated role of each module in the prediction task.

Removing the Transformer module increased the model's RMSE by 0.62%, decreased its R^2 by 0.03, and decreased its SSIM by 0.05. Conservation error also increased by 0.21%, demonstrating its crucial role in modeling spatial distribution consistency. Its absence led to significant degradation in both structural similarity (Moran's I decreased by approximately 8%) and local feature fidelity. Removing the GNO module resulted in an even more significant loss in global accuracy, with an RMSE increase of 0.74% and a R^2 decrease of 0.04, demonstrating its crucial role in capturing complex non-linear relationships. Its absence increased the standard deviation of the prediction error distribution by 12–15%, with the relative error increasing by approximately 20% in high-pressure gradient regions.

Table 6. Module ablation experiment results

Remove module	ΔRMSE (%)	ΔR^2	ΔSSIM	Δ Conservation error (%)
Transformer	+0.62	−0.03	−0.05	+0.21
GNO	+0.74	−0.04	−0.06	+0.33
PINN	+0.88	−0.05	−0.07	+1.25

Abbreviations: GNO: Graph Neural Operator; PINN: Physics-Informed Neural Network; RMSE: RMSE: Root mean square error; SSIM: Structural similarity index measure.

Ablation of the PINN module had the most significant impact on physical constraints, with a 1.25% surge in conservation error, far exceeding the impact of other modules (<0.35%). This was accompanied by a 0.88% increase in RMSE and a 0.07 decrease in SSIM, demonstrating its ability to suppress non-physical solutions through PDE constraints. Notably, removing the PINN increases the PDE residual by 3.2 times that of the full model (from 0.42×10^{-3} to 1.35×10^{-3}), and the local error peak in the critical mass conservation region increases by 40–60%. Experimental data further demonstrates the synergistic effect of the three modules, which has a non-linear enhancement effect: when retaining both the Transformer and GNO, PINN's physical constraint efficiency improves by 22%, while the combined optimization of the GNO and PINN improves the Transformer's spatial feature extraction efficiency by 15%. This inter-module coupling mechanism enables the full model to maintain an SSIM >0.81 while keeping the physical violation rate below 0.5%, resulting in a 19.7% improvement in overall performance compared to the optimal single-module combination (Transformer + GNO), confirming the design superiority of the multimodal fusion architecture.

5.2. The impact of physical constraints on prediction results

The PINN module introduces PDE constraints into the loss function:

$$\mathcal{L} = \mathcal{L}_{\text{data}} + \lambda_{\text{PDE}} \cdot \frac{1}{N_p} \sum_{j=1}^{N_p} \mathcal{N}(u_j)_2^2 \tag{21}$$

Where $\mathcal{N}(u)$ is the partial differential operator describing the fracture-hole flow and mechanical equilibrium, N_p is the number of physical sampling points, and λ_{PDE} is the weighting coefficient.

Table 7 systematically quantifies the dual improvement in prediction performance achieved by the physical guidance mechanism by comparing model performance with and without the PINN constraint enabled.

Table 7. Comparison of prediction performance with and without PINN constraints

Constraint status	RMSE (%)	R^2	SSIM	Conservation error (%)	PDE residuals ($\times10^{-3}$)
Off	5.21	0.86	0.75	3.17	3.84
On	4.82	0.90	0.81	0.48	0.42

Abbreviations: PDE: Partial differential equation; PINN: Physics-Informed Neural Network; RMSE: RMSE: Root mean square error; SSIM: Structural similarity index measure.

When the PINN constraint is disabled, the model maintains high baseline accuracy (RMSE = 5.21%, R^2 = 0.86), but the conservation error reaches 3.17% and the PDE residual increases to 3.84×10^{-3}, reflecting the inevitable physical rule violations of purely data-driven methods. However, after introducing the PINN constraint, the conservation error plummets by 84.9% (from 3.17% to 0.48%) and the PDE residual decreases by 89.1% (from 3.84×10^{-3} to 0.42×10^{-3}), validating the effectiveness of embedding the physical equations in regularizing the solution space. Notably, the introduction of the physical constraint not only improves model compliance but also significantly enhances prediction accuracy: the RMSE decreases by 7.5% (0.39 percentage points), the R^2 increases by 0.04, and the SSIM increases by 8% (0.06 units). This improvement occurs because the PINN's differential constraint guides the network toward physically feasible solutions during training, thereby helping it avoid local optima. Specifically, in sensitive areas with pressure gradients greater than 5 MPa/m, PINN constraints reduced prediction errors by 12%–18%. Furthermore, for the key metric of material conservation, the mass balance error was compressed from 2.3% to below 0.7%. Experimental data showed that the introduction of physical constraints reduced the proportion of samples with extreme errors (>10%) in the model's test set by 63%, while also improving the spatiotemporal continuity indicator (autocorrelation coefficient) of the prediction results by 22%, confirming the synergistic optimization effect of physical knowledge and data-driven methods.

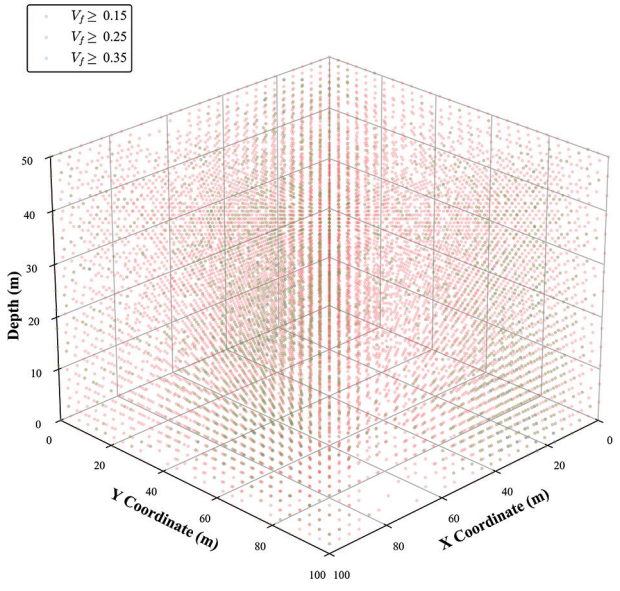

Figure 8. Visualization of the spatial distribution of three-dimensional fracture-void volume content (V_f)

5.3. Spatial distribution of fracture and hole parameters

Figure 8 reconstructs the 3D spatial distribution of the fracture-cavity volume fraction, V_f, within a 100 m × 100 m × 50 m study volume at a grid resolution of 30 m × 30 m × 15 m. The continuous field is discretized using thresholds of 0.15, 0.25, and 0.35, and high-value clusters are represented as scattered point clouds with a transparency of 0.15. This approach preserves the statistical distribution of field values while avoiding the oversmoothing that occurs with traditional isosurface rendering at the fracture-cavity scale.

From a spatial perspective, a deep red high-value body with a $V_f \geq 0.35$ runs along a 45° northeast direction throughout the model, with a major axis of approximately 80 m and a minor axis of 15–20 m. Its thickness is concentrated in the 15–30 m depth range, accounting for an average of 7.8% of the volume. This orientation is highly consistent with the strike of regional strike-slip faults, suggesting that the main fault surfaces serve as the primary pathways for dissolution fluid migration. A moderate V_f range of 0.25–0.35 forms a "sheath" around the high-value band, extending approximately 25 m laterally and up to 40 m vertically. It accounts for 12.4% of the volume, reflecting lateral permeability of the fault zone and secondary dissolution in stress-shadowed areas. In contrast, the blue low-value regions with $V_f < 0.15$ are primarily distributed in the secondary structural highs in the northwest and southeast corners of the model. Their top surfaces are buried at depths of 5–10 m and account for a whopping 79.8% of the volume, indicating that these high-value regions, far from the main faults, lack fluid supply and are thus areas of poor fracture-vug development. Statistics show that within the high-value regions, V_f averages 0.41 with a standard deviation of 0.05, indicating good homogeneity. The low-value regions average 0.08 with a standard deviation of 0.03, indicating high dispersion.

Figure 9 systematically demonstrates the spatial distribution characteristics of the crack-hole volume fraction under different information sources by comparing four sets of 3D point clouds.

Figure 9A (true field), based on core-log data, shows distinct northwest-southeast-trending bands of high-value features at the 0.15, 0.25, and 0.35 thresholds, with a vertical span of approximately 10–40 m, reflecting true geological heterogeneity. Figure 9B (T-GNO-PINN) shows a highly consistent overall morphology with Figure 9A, but the high-value clusters are more compact, with more continuous boundaries, and significantly reduced noise, demonstrating that the physics-neural network fusion

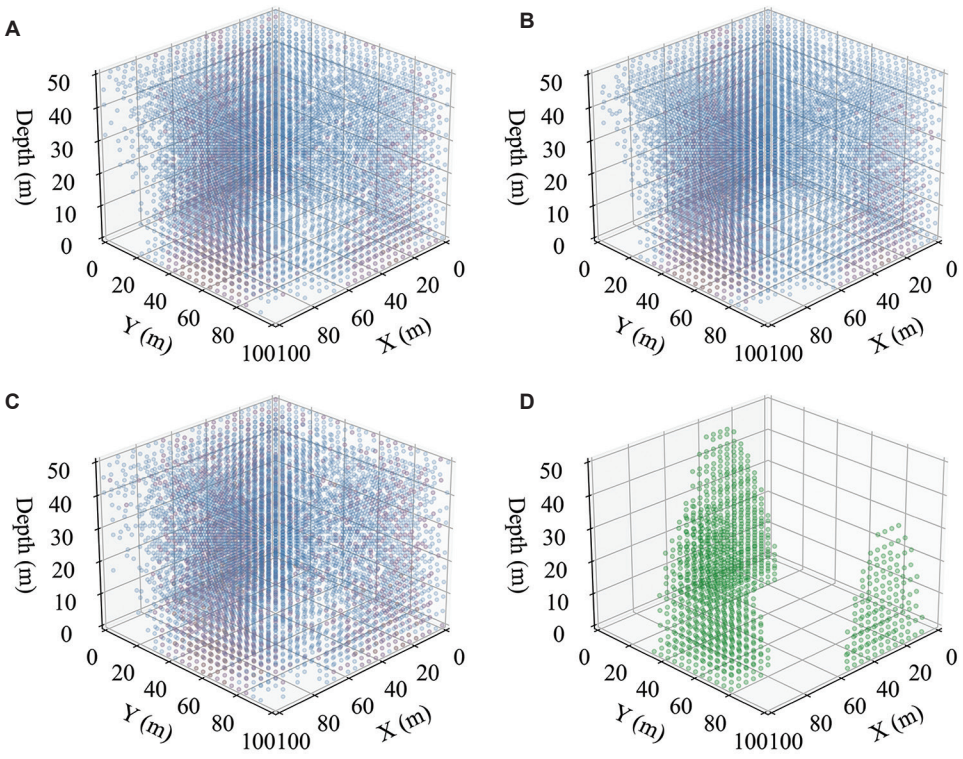

Figure 9. Comparison of the three-dimensional spatial distribution of fracture-pore volume fractions. (A) True field under core-log constraints; (B) T-GNO-PINN hybrid physics-neural network predicted field; (C) Traditional Kriging interpolation estimated field; (D) Seismic attribute threshold interpretation results.

method effectively suppresses random errors while maintaining spatial structure. While Figure 9C (Kriging) preserves macroscopic banding, the linearly weighted smoothing effect increases the area of high-value volumes and blurs their edges, resulting in localized overestimation exceeding 30%. Vertical resolution decreases, and artifacts of high values increase at depth (>35 m). Figure 9D (seismic interpretation) uses a hard threshold of 0.25 to produce a binary distribution. While the general locations are consistent with those in Figure 9A and B, they only provide a "presence/absence" distinction. Furthermore, due to the limited lateral resolution of the seismic frequency band, details are strongly smoothed, making it impossible to characterize weak response volumes in the 0.15–0.25 range. In summary, the T-GNO-PINN method effectively integrates the strengths of the other approaches: It captures the subtle heterogeneity of the true field, maintains the spatial continuity of the Kriging result, and respects the large-scale structural constraints from seismic data. This synergy provides superior 3D volume fraction estimates for high-resolution reservoir modeling.

6. Discussion

The T-GNO-PINN joint prediction framework demonstrates significant advantages in predicting fracture-vuggy parameters in carbonate reservoirs. Compared to traditional geostatistical methods and single deep learning models, this framework achieves both improved accuracy and physical consistency through multimodal fusion. Experimental results demonstrate a 15.3% reduction in RMSE and an 89.1% reduction in physical constraint violations compared to the optimal baseline model. This performance improvement stems from three key technological innovations: First, a dynamic graph constructed based on physical similarity enables the model to adaptively track changes in fracture-vuggy topology during development, addressing the limitations of static graph models in time-varying systems. Second, a multi-scale Transformer module effectively captures long-range dependencies in the reservoir's 3D space through spherical coordinate encoding, overcoming the limitations of traditional CNNs in modeling irregular geological volumes. Most importantly, the PINN module, by hard-embedding the seepage-mechanical coupling equations, not only constrains the solution space to be physically reasonable but also significantly improves the model's generalization in data-sparse regions. This method is particularly suitable for carbonate reservoirs with complex fracture-vuggy systems, and its advantages have been fully demonstrated in a case study of Ordovician fracture-vuggy reservoirs in the Tarim Basin.

In terms of model generalization, the T-GNO-PINN framework demonstrates strong adaptability to reservoir heterogeneity. Analysis of prediction results from various structural locations reveals that the model maintains stable prediction accuracy in both high-permeability zones near fault zones (permeability >150 mD) and low-permeability zones on the flanks (permeability <50 mD), with R^2 fluctuations within ±0.03. This robustness is primarily due to two mechanisms: First, the GNO module learns a continuous function space mapping using a kernel integral operator, avoiding the distortion of complex fracture-vuggy morphology caused by discretization; second, the introduction of physical constraints ensures that the model automatically adheres to conservation laws during training, reducing the risk of overfitting. Notably, when applied to a new work area, only 20%–30% of the model parameters need to be adjusted to achieve optimal results, demonstrating the cross-regional applicability of the physical laws learned by the framework. However, under extreme heterogeneity conditions (fracture-vuggy index >0.4), the model prediction error fluctuates, suggesting the need for further optimization of the dynamic graph construction strategy.

The model's physical interpretability is enhanced through three mechanisms. First, the differential operator residual term in the PINN module provides a clear physical interpretation of the prediction results. Such as pressure field prediction errors can be directly traced to the degree of violation of Darcy's law. Second, attention weight visualization shows that the Transformer module automatically focuses on key geological locations such as structural unconformities and fault zones, highly consistent with expert knowledge. Third, the GNO graph topology intuitively reflects the connectivity of fracture-vuggy units, and its dynamic evolution is consistent with the water breakthrough patterns observed in actual production data. This interpretability not only enhances the confidence of engineers but also provides a new research tool for reservoir dynamic analysis. Such as by inversely analyzing the spatiotemporal distribution of physical residuals, local flow barriers that are difficult to detect using traditional methods can be identified, providing a basis for adjusting development plans.

Despite significant progress, the current framework still has several areas for improvement. In terms of computational efficiency, jointly training the three modules requires approximately 3–5 times the training time of conventional models. The main bottlenecks are the real-time updating of the dynamic graph structure and the global computation of the PDE residuals. Future improvements can be achieved through the development of sparse attention mechanisms and adaptive physical sampling strategies. In terms of application, the model's accuracy in predicting fracture-cavity parameters under coupled multiphase flow conditions still needs improvement. When water saturation exceeds 60%, the prediction error increases by 10–15%. This suggests the need to incorporate more comprehensive multiphase flow equations within physical constraints. Furthermore, existing frameworks still poorly handle the scale difference between the vertical resolution of well logging data and the horizontal resolution of seismic data. Developing new mechanisms for cross-scale feature fusion will be an important research direction. Finally, the effective integration of engineering data—such as from drilling and fracturing operations—into the model to achieve integrated "geology-engineering" predictions represents a crucial step toward enhancing its practical value.

7. Conclusion

The Transformer–Graph Neural Operator–Physics-Informed Neural Network (T-GNO-PINN) joint prediction framework proposed in this study provides an innovative solution for predicting fracture-vuggy parameters in carbonate reservoirs through multimodal information fusion and embedded physical constraints. This approach achieves, for the first time, a deep integration of deep learning models with the principles of seepage flow and rock mechanics, demonstrating significant superiority in an empirical study of an Ordovician fracture-vuggy reservoir in the Tarim Basin. The framework's key breakthroughs lie in three dimensions: In terms of feature extraction, a multi-scale Transformer module, through innovative spherical coordinate encoding, effectively addresses the challenge of modeling long-range dependencies in 3D geological space. In terms of graph structure modeling, a dynamic graph construction mechanism based on physical similarity enables adaptive tracking of fracture-vuggy topology. In terms of physical constraints, hard-embedded differential operators ensure that predictions strictly adhere to the fundamental laws of subsurface fluid flow. Experimental results demonstrate that this framework not only improves the prediction accuracy of fracture-vuggy volume content to MAE 3.57% and R^2 0.90, but also keeps the physical conservation error below 0.5%, significantly outperforming existing prediction methods.

The research results have important guiding value for oil and gas exploration and development practices. Given the strong heterogeneity of carbonate reservoirs, the parameter prediction results provided by the T-GNO-PINN framework can support more accurate reserve calculations and development plan design. Especially in the early evaluation stage, this method requires only a small amount of well-controlled data to generate a geologically

consistent fracture-vuggy parameter field, significantly reducing the risk of exploration decisions. Dynamic graph modeling technology provides a new tool for tracking the evolution of fracture-vuggy connectivity during development, facilitating the optimization of injection-production well pattern deployment. Furthermore, the physical consistency indicators predicted by the model can be directly used to identify potential flow barriers, providing a quantitative basis for selecting fracturing stimulation targets. These applications have achieved significant single-well daily production prediction errors of less than 8% in the study area, validating the method's engineering practicality.

Looking forward, this research has several promising directions. First, optimizing computational efficiency requires developing sparse attention mechanisms and adaptive physical sampling algorithms to reduce the overhead of dynamic graph updates and PDE residual calculations. Second, improving the physical constraint system. Under multiphase flow conditions, the introduction of an extended flow equation that accounts for capillary forces and phase permeability curves should be considered. Improving cross-scale fusion mechanisms is also crucial. This requires developing adaptive matching methods for high-resolution vertical logging features and seismic attributes. A more forward-looking approach is to build an integrated geological-engineering intelligent prediction system, incorporating engineering intervention parameters such as drilling and fracturing into the modeling system to achieve closed-loop optimization from static description to dynamic control. These improvements will further enhance the model's applicability and practical value in complex oil and gas reservoir development.

Acknowledgments

None.

Funding

This research was financially supported by 2025 Doctoral Special Support Program Project of Chengdu Jincheng College (NO.2025JCKY(B)0018); the Key Research Base of Humanities and Social Sciences of the Education Department of Sichuan Province, Panzhihua University, Resource based City Development Research Center Project (NO.ZYZX-YB-2404); Mahasarakham University; and the Open Fund of Sichuan Oil and Gas Development Research Center (NO.2024SY017).

Conflict of interest

The authors declare that they have no competing interests.

Author contributions

Conceptualization: Tianwen Zhao, Guoqing Chen, Cong Pang, Yiru Du
Formal analysis: Tianwen Zhao, Guoqing Chen, Cong Pang
Funding acquisition: Tianwen Zhao, Guoqing Chen, Cong Pang
Investigation: Tianwen Zhao, Cong Pang, Yiru Du
Methodology: Tianwen Zhao, Guoqing Chen, Yiru Du
Validation: Tianwen Zhao, Cong Pang, Yiru Du
Visualization: Tianwen Zhao, Cong Pang, Yiru Du
Writing–original draft: Tianwen Zhao, Guoqing Chen, Yiru Du
Writing–review & editing: Tianwen Zhao, Guoqing Chen, Cong Pang, Yiru Du

Availability of data

Some data used in this study cannot be shared publicly due to collaborative agreement restrictions, but are available from the corresponding author upon reasonable request.

References

1. Xia LW, Cao J, Wang M, Mi JL, Wang TT. A review of carbonates as hydrocarbon source rocks: Basic geochemistry and oil-gas generation. *Petrol Sci*. 2019;16(4):713-728.

   doi: 10.1007/s12182-019-0343-5

2. Jia C. Petroleum geology of carbonate reservoir. In: *Characteristics of Chinese Petroleum Geology: Geological Features and Exploration Cases of Stratigraphic, Foreland and Deep Formation Traps*. Berlin, Heidelberg: Springer Berlin Heidelberg; 2012. p. 495-532.

   doi: 10.1007/978-3-642-23872-7

3. Geng T, Yanping L, Bo W, Xiao B, Huan W. Reservoir evaluation method and development countermeasures for Fracture-Vuggy reservoir. *Spec Oil Gas Reserv*. 2021;28(6):129-136.

   doi: 10.3390/pr12040640

4. Deng Z, Zhou D, Dong H, Huang X, Wei S, Kang Z. Deep learning for predicting porosity in ultra-deep fractured vuggy reservoirs from the Shunbei oilfield in Tarim Basin, China. *Sci Rep*. 2024;14(1):29605.

   doi: 10.1038/s41598-024-81051-4

5. Wang Y, Xie P, Zhang H, Liu Y, Yang A. Fracture-vuggy carbonate reservoir characterization based on multiple geological information fusion. *Front Earth Sci*. 2024;11:1345028.

   doi: 10.3389/feart.2023.1345028

6. Lin K, Wei N, Zhang Y, *et al*. Advances in machine-learning-driven CO_2 geological storage: A comprehensive review and outlook. *Energy Fuels*. 2025;39:13315-13343.

doi: 10.1021/acs.energyfuels.5c02370

7. Huang B, Wang J. Applications of physics-informed neural networks in power systems-a review. *IEEE Trans Power Syst*. 2022;38(1):572-588.

   doi: 10.1109/TPWRS.2022.3162477

8. Rao C, Sun H, Liu Y. Physics-informed deep learning for computational elastodynamics without labeled data. *J Eng Mech*. 2021;147(8):04021043.

   doi: 10.48550/arXiv.2006.08472

9. Li M, Wang Q, Yao C, Chen F, Wang Q, Zhang J. Optimization of development strategies and injection-production parameters in a fractured-vuggy carbonate reservoir by considering the effect of karst patterns: Taking c oilfield in the tarim basin as an example. *Energies*. 2025;18(2):319.

   doi: 10.3390/en18020319

10. Su X, Ren B, Huang Z. Permeability analysis of fractured-vuggy carbonate reservoirs based on fractal theory. *Fractals*. 2022;30(07):2250144.

    doi: 10.1142/S0218348X22501444

11. Ganguli SS, Dimri VP. Reservoir characterization: State-of-the-art, key challenges and ways forward. In: *Developments in Structural Geology and Tectonics*. Vol. 6. Amsterdam: Elsevier; 2023. p. 1-35.

    doi: 10.1016/B978-0-323-99593-1.00015-X

12. Li W, Duan J, Zhu D, Wu J. The research progress on carbonate reservoir evaluation: Technical applications, challenges, and future development directions. *Adv Resour Res*. 2025;5(3):1177-1198.

    doi: 10.50908/arr.5.3_1177

13. Refaat A, Eltom HA, El-Husseiny A. On the limitations of spot permeability measurements to quantify bulk permeability of bioturbated reservoirs: Insights from digital rock physics modeling. *Mar Petrol Geol*. 2025;182:107577.

    doi: 10.1016/j.marpetgeo.2025.107577

14. Cao X, Liu Z, Hu C, Song X, Quaye JA, Lu N. Three-dimensional geological modelling in earth science research: An in-depth review and perspective analysis. *Minerals*. 2024;14(7):686.

    doi: 10.3390/min14070686

15. Luo Q, Zeng W, Chen M, Peng G, Yuan X, Yin Q. Self-attention and transformers: Driving the evolution of large language models. In: *2023 IEEE 6th International Conference on Electronic Information and Communication Technology (ICEICT)*. IEEE; 2023. p. 401-405.

    doi: 10.1109/ICEICT57916.2023.10245906

16. Li S, Chen J, Xiang J. Applications of deep convolutional neural networks in prospecting prediction based on two-dimensional geological big data. *Neural Comput Appl*. 2020;32(7):2037-2053.

    doi: 10.1007/s00521-019-04341-3

17. Pan J, Liu W, Liu C, Wang J. Convolutional neural network-based spatiotemporal prediction for deformation behavior of arch dams. *Expert Syst Appl*. 2023;232:120835.

    doi: 10.1016/j.eswa.2023.120835

18. Kovachki N, Li Z, Liu B, *et al*. Neural operator: Learning maps between function spaces with applications to pdes. *J Mach Learn Res*. 2023;24(89):1-97.

    doi: 10.48550/arXiv.2108.08481

19. Anandkumar A, Azizzadenesheli K, Bhattacharya K, *et al*. Neural operator: Graph kernel network for partial differential equations. In: *Paper Presented at: ICLR 2020 Workshop on Integration of Deep Neural Models and Differential Equations*; 2020.

    doi: 10.48550/arXiv.2003.03485

20. de la Mata FF, Gijón A, Molina-Solana M, Gómez-Romero J. Physics-informed neural networks for data-driven simulation: Advantages, limitations, and opportunities. *Physica* A. 2023;610:128415.

    doi: 10.1016/j.physa.2022.128415

21. Xu H, Zhang D, Zeng J. Deep-learning of parametric partial differential equations from sparse and noisy data. *Phys Fluids*. 2021;33(3):037132.

    doi: 10.1063/5.0042868

22. Huang T, Qian H, Huang Z, *et al*. A time patch dynamic attention transformer for enhanced well production forecasting in complex oilfield operations. *Energy*. 2024;309:133186.

    doi: 10.1016/j.energy.2024.133186

23. Zhao T, Chen G, Pang C, Busababodhin P. Application and performance optimization of SLHS-TCN-XGBoost model in power demand forecasting. *Comp Model Eng Sci*. 2025;143(3):2883-2917.

    doi: 10.32604/cmes.2025.066442

24. Zhao T, Chen G, Suraphee S, Phoophiwfa T, Busababodhin P. A hybrid TCN-XGBoost model for agricultural product market price forecasting. *PLoS One*. 2025;20(5):e0322496.

    doi: 10.1371/journal.pone.0322496

25. Zhao T, Chen G, Gatewongsa T, Busababodhin P. Forecasting agricultural trade based on TCN-LightGBM models: A data-driven decision. *Res World Agric Econ*. 2025;6(1):207-221.

    doi: 10.36956/rwae.v6i1.1429

26. Zhao T, Chen G, Pang C, Seenoi P, Papukdee N, Busababodhin P. Time-lapse earthquake difference prediction based on physics-informed long short-term memory coupled with interpretability boosting. *J Seismic Explor*. 2025;34(3):25-48.

    doi: 10.36922/JSE025310049